

Volume *Functional MRI*

Edited by S.H. Faro and F.B Mohamed

Springer-Verlag New York (2002)

Chapter 1. Principles of Functional MRI

Seong-Gi Kim, Ph.D. and Peter A. Bandettini, Ph.D.

Department of Neurobiology, University of Pittsburgh, Pittsburgh PA &

National Institute of Mental Health, NIH, Bethesda, MD

Correspondence to

Seong-Gi Kim

University of Pittsburgh,

Department of Neurobiology,

3025 Carson Street,

Pittsburgh, PA 15203

Contents

- 1.1. Introduction
- 1.2. Physiological Changes
- 1.3. Functional Imaging Contrasts
- 1.4. T_1 -weighted fMRI
- 1.5. T_2^* - and T_2 -weighted fMRI
 - 1.5.1. Intravascular Component
 - 1.5.2. Extravascular Component
 - 1.5.3. Sping-echo vs. Gradient-echo BOLD
- 1.6. Contrast-to-noise Ratio
- 1.7. Spatial and Temporal Resolution of fMRI
 - 1.7.1. Spatial Resolution
 - 1.7.2. Temporal Resolution
- 1.8. Conclusions
- 1.9. References

1.1. Introduction

The idea that regional cerebral blood flow (CBF) could reflect neuronal activity began with experiments of Roy and Sherrington at 1890 ¹. This concept is the basis for all hemodynamic-based brain imaging techniques being used today. The focal increase in CBF can be considered to directly relate to neuronal activity because the glucose metabolism and CBF changes are closely coupled ². Thus, the measurement of CBF change induced by stimulation has been used for mapping brain functions. Because cerebral metabolic rate of glucose (CMRglu) and CBF changes are coupled, it is assumed that cerebral metabolic rate of oxygen (CMRO₂) and CBF changes are also coupled. However, Fox and colleagues reported, based on positron emission tomographic measurements of CBF and CMRO₂ in humans during somatosensory and visual stimulation ^{3,4}, that an increase in CBF increase surpassed an increase in CMRO₂. Consequently, a mismatch between CBF and CMRO₂ changes results in an *increase* in the capillary and venous oxygenation level, opening a new physiological parameter (in addition to CBF change) for brain mapping. In 1990, based on rat brain studies during global stimulation at 7T, Ogawa and colleagues at AT&T Bell Laboratories reported that functional brain mapping is possible by using the venous blood oxygenation level-dependent (BOLD) magnetic resonance imaging (MRI) contrast ⁵⁻⁷. The BOLD contrast relies on changes in deoxyhemoglobin (dHb), which acts as an endogenous paramagnetic contrast agent ^{5, 8}. Therefore, changes in the local dHb concentration in the brain lead to alterations in the signal intensity of magnetic resonance images (MRI) ^{5-7, 9}.

Application of the BOLD contrast to human functional brain mapping followed shortly¹⁰⁻
¹². Since then, functional magnetic resonance imaging (fMRI) has been the tool of choice for visualizing neural activity in the human brain. The fMRI has been extensively used for investigating various brain functions including vision, motor, language and cognition. The BOLD imaging technique is widely used because of its high sensitivity and easy implementation. Since the BOLD signal is dependent on various anatomical, physiological, and imaging parameters¹³, its interpretation with respect to physiological parameters is qualitative or semi-quantitative. Thus, it is difficult to compare the BOLD signal changes in different brain regions, from the different imaging laboratories, and/or from different magnetic fields. Alternatively, change in CBF can be measured using MRI. Since these fMRI signals are related to a single physiological parameter, its quantitative interpretation is more straightforward.

Functional MRI is a very powerful method to map brain functions with relatively high spatial and temporal resolution. In order to utilize fMRI techniques efficiently and interpret fMRI data accurately, it is important to examine underlying physiology and physics. In this book chapter, we will discuss the signal source of the BOLD signal and improvement of BOLD fMRI techniques.

1.2. Physiological Changes

Since fMRI measures the vascular hemodynamic response induced by increased neural activity, it is important to understand a chain of events from task to fMRI (see Fig. 1). Task and/or stimulation induce synaptic and electric activities at localized regions, which will trigger an increase in CBF, cerebral blood volume (CBV), CMR_{O_2} , and CMR_{glu} . Although the exact

relationship between neural activity and vascular physiology change is not known, it is well-accepted that the change in CMR_{glu} is a good indicator of neural activity. Since the CMR_{glu} change is linearly correlated with the CBF change, a change in CBF is an alternative, good secondary indicator of neural activity.

CBF and CBV changes are inter-correlated since change in CBF is a multiple of CBV and velocity changes. The relationship between CBF and CBV obtained in monkeys during CO_2 modulation can be described as

$$\Delta \text{CBV} / \text{CBV} = \Delta \text{CBF} / \text{CBF} \cdot 1.38 \quad [1]$$

where $\Delta \text{CBV} / \text{CBV}$ and $\Delta \text{CBF} / \text{CBF}$ are relative total CBV and CBF changes¹⁴. The similar relationship was observed in rat brain during hypercapnia (see Fig. 2a)¹⁵. Recently, Ito et al. measured relative CBF and CBV changes in human visual cortex during visual stimulation, and found that the above relationship is also applicable to human stimulation studies¹⁶. Thus, change in total blood volume can be a good index of the CBF change. Change in total blood volume can be measured by using contrast agents because contrast agents distribute in all vascular system. Since venous blood volume constitutes of 75% of the total blood volume¹⁵, it is conceivable that the venous blood volume change is dominant. However, based on separate measurements of arterial and venous blood volume changes during hypercapnia by a novel ^{19}F NMR technique and video-microscopy, a relative change in venous blood volume is approximately a half of the relative total CBV change induced by rigorous dilation of arterial vessels (see Fig. 2b)¹⁵.

In the context of BOLD contrast, only venous blood can contribute to activation-induced susceptibility changes since venous blood contains deoxyhemoglobin. The venous oxygenation level is dependent on a mismatch between oxygen supply by CBF and oxygen utilization in tissue. Assuming an arterial oxygen saturation of 1.0, the relative change of venous oxygenation level (Y) can be determined from the relative changes of both CBF and $CMRO_2$ in the following manner¹⁷:

$$\frac{\Delta Y}{1 + Y} = 1 - \frac{\Delta CMRO_2 / CMRO_2}{\Delta CBF / CBF} \quad (2)$$

From Eq. [2], a relative change in $CMRO_2$ can be obtained from information of relative CBF and Y changes. It is also important to recognize that relationship between oxygenation change and blood flow change is linear at low CBF changes^{18, 19}, but non-linear at very high CBF changes^{20, 21}.

1.3. Functional Imaging Contrasts

MRI signal in a given voxel can be described as a vector sum of signals from different compartments. Thus, MRI signal intensity is

$$S = \sum_i S_{oi} \exp(-T_{1i}^*/T_1) \exp(-T_{2i}^*/T_2) \quad [3]$$

where S_{oi} is the spin density of compartment i in a given voxel, and T_{1i}^* and T_{2i}^* are apparent longitudinal and transverse relaxation times of compartment i , respectively. Thus, the signal change can be induced by a change in spin density, T_1^* , and/or T_2^* . Changes in T_1^* can be induced by CBF changes and changes in T_2^* can be induced by modulation in paramagnetic contents.

1.3.1. T_1 -weighted fMRI

An inflow effect into the region of interest will shorten apparent T_1 . Using this property, time-of-flight angiographic images can be obtained. When the inflow time is relatively long such as one second, the inflow effect exists not only in arterial vessels and in capillaries and surrounding tissue. Thus, CBF can be measured non-invasively using arterial water as a perfusion tracer²²⁻²⁷. The general principle behind the arterial spin labeling (ASL) techniques is to differentiate the net magnetization of endogenous arterial water flowing proximally to the region of interest from the net magnetization of tissue. Labeled spins by RF pulse(s) move into capillaries in the imaging slice and exchange with tissue water spins. These techniques include continuous arterial spin tagging²², flow-sensitive alternating inversion recovery (FAIR)²³⁻²⁵, and various other techniques²⁶⁻²⁸. In all of these techniques, two images are acquired, one with arterial spin labeling and the other without labeling. Among many available techniques, the FAIR is most widely utilized because of its simple implementation. Two IR images are acquired in FAIR; one with a non-slice-selective inversion pulse and the other with a slice-selective inversion pulse. The longitudinal magnetization following a non-selective inversion pulse and a slice-selective inversion pulse recover by $R_1 (=1/T_1)$ and $R_1^* (=1/T_1^*)$, respectively, where R_1^* is equal to $R_1 + CBF/\lambda$ where λ is the tissue-blood partition coefficient ((g water/g tissue)/(g water/ml blood)). Figure 3 shows hypothetical relaxation recovery curves after the inversion pulse with and without the inflow effect. CBF can be estimated by determinations of T_1 and T_1^* . In functional activation studies, two IR images are alternately and repeatedly acquired during both control and task periods. Then the differences between each pair of slice-selective and non-selective IR images are calculated during control periods (ΔS_{cont}) and stimulation periods (ΔS_{st}).

Relative CBF changes during task periods can be described as $CBF_{st}/CBF_{cont} = \Delta S_{st}/\Delta S_{cont}$ where CBF_{st} and CBF_{cont} are the CBF during task and control periods, respectively. Functional brain mapping has been successfully obtained during motor, vision and cognitive tasks (see Figure 4 for finger movements). Relative CBF changes measured by FAIR agree extremely with those measured by $H_2^{15}O$ positron emission tomography (PET) in the same region and subject during the identical stimulation task ²⁹. Thus, the perfusion-weighted MRI technique is an excellent approach to detect relative CBF changes induced by neural activity or other external perturbations. Further, since small arterioles and capillaries are very close to neuronally active tissue, it is expected that tissue-specific CBF signal improves a spatial specificity of functional images. Figure 5 demonstrates the signal specificity of the perfusion-weighted fMRI technique in an anesthetized cat during single-orientation stimuli. Based on previous 2-DG glucose studies ³⁰, CMRglu maps showed patchy, irregular columnar structures with an average inter-column distance of 1.1-1.4 mm. CBF-based fMRI maps showed similar activation patterns and inter-cluster distance, suggesting that the CBF response is specific to areas with metabolic increase ³¹. It should be noted that the sagittal sinus running between two hemispheres does not show signal changes in CBF-based studies, contrary to conventional BOLD measurements, which has showed the largest signal change in the draining sagittal sinus ^{32, 33}.

Although perfusion-based approaches can be utilized for fMRI studies, there are many shortcomings. First, large vascular contribution exists because labeled blood fill up arterial vasculature before it travels into capillaries (see also Figure 10) ³⁴. This arterial vascular contribution can be reduced by using spin-echo data collection (see Fig. 10) or eliminated using bipolar gradients, but this reduces SNR of perfusion-weighted images. Since the dilation of

large arterial vessels is small ¹⁵, we did not find activation at large vessel areas ³⁵. Thus, for mapping purpose, it may not be necessary to remove large vessel contributions (see Fig. 5). Second, the proper perfusion contrast is only achieved when enough time is allowed for the labeled arterial spins to travel into the region of interest and exchange with tissue spins. This makes it difficult to detect changes in CBF with a temporal resolution greater than T_1 of arterial blood, resulting in ineffective signal averaging. Third, in multi-slice application, transit times to different slices are different, which may cause errors in quantification of relative CBF changes ^{28, 36}. Relative CBF changes measured by multi-slice FAIR agree extremely with those measured by $H_2^{15}O$ positron emission tomography (PET), suggesting that the change in transit time is not a significant confound ²⁹.

1.3.2. T_2^* and T_2 -based fMRI

It is well known that, with typical fMRI acquisition parameters, the BOLD response is particularly sensitive in and around large draining veins because the BOLD effect is sensitive to baseline venous blood volume, and to vessel size ^{17, 37}. To understand the spatial resolution of BOLD-based fMRI, it is important to examine the anatomical source of the BOLD signal. The BOLD contrast induced by dHb arises from both intravascular (IV) and extravascular (EV) components. Since the exchange of water between these two compartments (typical lifetime of the water in capillaries $> 500\text{msec}$) is relatively slower compared with the imaging time (echo time $< 100\text{ ms}$), MRI signals from these are treated as separate pools.

3.2.1 Intravascular Component

During fMRI measurements, water rapidly exchanges between red blood cells (RBC) with paramagnetic dHb and plasma (average water residence time in RBCs = ~5 ms) and move along space with different fields by diffusion (e.g., diffusion distance (i.e., $(6 \times \text{diffusion constant} \times \text{diffusion time})^{1/2}$) during ~50 ms measurement time = ~17 μ m with diffusion constant of ~1 μ m²/ms). Thus, ‘dynamic’ (time irreversible) averaging occurs over the many different fields induced by dHb. All water molecules inside the vessel will experience the similar ‘dynamic averaging’, resulting in reduction of T_2 of blood water in the venous pool. A transverse relaxation rate of blood water is affected by exchange of water and diffusion. In both cases, blood T_2 can be written as

$$1/T_2 = A_0 + K(1-Y)^2 \quad [4]$$

where A_0 is a field independent constant term and K would scale quadratically with the magnetic field and depend also on the echo time used in a spin echo measurement³⁸. T_2 of blood water at 1.5T is ~127 ms for $Y = 0.6$ ³⁸, while T_2 is ~12-15 ms at 7T^{39, 40} and 5 ms at 9.4 T⁴¹. These experimental values are consistent with predictions based on Eq. [4]. T_2 values of gray matter water at 1.5T, 7T, and 9.4 T are 90 ms⁴², 55 ms⁴⁰, and 40 ms⁴¹, respectively. When spin-echo time is set to T_2 of gray matter, it is evident that the blood contribution to MRI signal decreases dramatically when magnetic field increases.

In addition to the T_2 change induced by deoxyhemoglobin, frequency shift is observed. When a blood vessel is considered as an infinite cylinder?? frequency shift ?? induced by dHb within and around the vessel is depicted at Fig. 6. It should be noted that frequency and magnetic field are interchangeable because $\omega = \gamma B$ where γ is the gyromagnetic ratio and B is the magnetic field. Inside the blood vessel, the frequency shift will be expressed by ? ?

$$\Delta \omega_{in} = 2\pi \Delta \chi (1-Y) \gamma_0 (\cos^2 \theta - 1/3) \quad [5]$$

where $\Delta \chi$ is the maximum susceptibility difference between fully oxygenated and fully deoxygenated blood, Y is the fraction of oxygenation in venous blood, γ_0 is the applied magnetic field of magnet in frequency units ($\gamma_0 = \gamma B_0$), and θ is the angle between the applied magnetic field (B_0) and vessel orientation. $\Delta \chi$ is dependent on a hematocrit level. Assuming a hematocrit level of 0.38 and the susceptibility difference between 100% oxyhemoglobin and 100% dHb of 0.27 ppm⁸, $\Delta \chi$ in whole blood is 0.1 ppm. In a given voxel, many vessels with different orientations exist. Rather than inducing a net phase shift, the random orientations cause a phase dispersion, therefore causing a reduction in T_2^* . However, a very large vessel will have its own phase depending on oxygenation level and orientation. Using this property, Haacke and his colleagues determined a venous oxygenation level⁴³ from a vessel that they determined to be perpendicular to B_0 .

1.3.2.2. Extravascular Component

At any location outside the blood vessel, the frequency shift can be described by

$$\Delta \omega_{out} = 2\pi \Delta \chi (1-Y) \gamma_0 (a/r)^2 (\sin^2 \theta) (\cos 2\theta) \quad [6]$$

where a is the radius of blood vessel, r is the distance from the point of interest to the center of the blood vessel, and θ is the angle between r and plane defined by B_0 and the vessel axis. The dephasing effect is dependent on the orientation of vessel. Vessels running parallel to the magnetic field do not have the EV effect, while those orthogonal to B_0 will have the maximal effect (see Fig. 7). At the lumen of vessels ($r = a$), $\Delta \omega_{out}$ is identical and independent of vessel sizes. At $r = 5a$, the susceptibility effect is 4% of the maximally available $\Delta \omega_{out}$. The same

frequency shift will be observed at 15 μ m around a 3- μ m radius capillary and 150 μ m around a 30- μ m radius venule (see Fig. 8). This shows that the dephasing effect around a larger vessel is more spatially extensive because of a smaller susceptibility gradient. The EV contribution from large vessels to conventional BOLD signal is significant, regardless of magnetic field strength⁴¹. During echo time for fMRI studies (e.g., ~50 ms), water molecules diffuse ~17 μ m, which covers a space with the entire range of susceptibility effects around the 3- μ m radius capillary, but with a small range of static susceptibility effects around the 30- μ m radius venule. Thus, tissue water around *capillaries* will be ‘dynamically’ averaged over the many different fields (i.e., no net phase change like the IV component). However, because tissue water around *large vessels* will be locally averaged during an echo time, the static dephasing effect is dominant (see small circles with dephasing information in Figure 8). The dephasing effect around large vessels can be refocused by the 180° RF pulse. Therefore, the EV contribution of large vessels can be reduced by using the spin-echo technique (see Fig. 7).

In a given voxel, MRI signal intensity with dephasing effects (i.e., frequency shifts) induced by numerous vessels will be summed, resulting in a decrease in T_2^* and a decrease in MRI signal. Signal in the voxel can be described, according to equation

$$S(TE) = \sum_i S_0 e^{-TE/T_{2i}} e^{i\phi_i TE} \quad [7]$$

where the summation is performed over the parameter i , which designates small volume elements within the voxel (e.g., hypothetically a volume with a small circle with phase shift); the time-averaged magnetic field experienced within these small volume elements. $\phi_i TE$ indicates the phase shift of location i at echo time TE. This signal loss occurs from “*static averaging*”.

If the variation Δf_i within the voxel is relatively large, signal will be decayed approximately with a single exponential time constant T_2^* . Based on Monte Carlo simulation, the dephasing effect within a voxel can be simplified into R_2' (in order to separate measured $R_2^* = \text{intrinsic } R_2 + R_2'$ induced by contrast agent) change as

$$R_2' = \text{CBV} \cdot \Delta f^2 \cdot (1 - Y)^{\alpha} \quad [8]$$

where Δf and α are constants^{17,44,45}. The power term α is 1.0 for 'static' averaging domain and 2.0 for time-irreversible averaging domain^{17,44,45}. All venous vessels will have a power term of 1.0 – 2.0; α is 1.0 – 2.0 for the gradient-echo sequence, and 1.5-2.0 for spin-echo sequence^{17,44,45}. If diffusion-related travel distance of water molecules during echo time is sufficient to effectively average frequency shifts (also related to magnetic field), α will be 2.0. Thus, a longer echo time (i.e., longer diffusion distance) and a higher magnetic field (i.e., large susceptibility gradient) will reduce a vessel size for dynamic averaging. Figure 9 shows the R_2' dependency on vessel size and frequency shift, which was obtained from Monte Carlo simulation with CBV of 2% and echo time of 40 ms. R_2' increases linearly with venous CBV¹⁷. Frequency shift at $Y = 0$ is 40 Hz at 1.5T and 107 Hz at 4T. Let's examine vessels with 3 μm and 30 μm radii. When a frequency shift increases from 32 to 64 Hz (due to an increase in magnetic field and/or a decrease in oxygenation level), R_2^* values of 3 μm and 30 μm radius vessels change from 1.2 to 3.5 sec^{-1} and from 2.8 to 6.0 sec^{-1} , respectively. A power term α will be 1.5 for a 3 μm vessel and 1.1 for a 30 μm vessel, showing that a smaller size vessel is more sensitive to the frequency shift (such as induced by magnetic field). Spin-echo and gradient-echo BOLD signal changes in a function of vessel size can be seen in Fig. 9⁴⁶. At capillaries, a change in R_2 is similar to that of R_2^* . However, when vessel size increases above 5-8 μm diameter (which is related to diffusion time and susceptibility gradient), R_2 change is reduced, but R_2^* change remains high. Thus,

spin-echo BOLD signals predominantly originate from small-size vessels including capillaries, while gradient-echo BOLD signals dominate from large draining veins.

1.3.2.3. Spin-echo vs. Gradient-echo BOLD

As we discussed already, gradient-echo BOLD signals consist of EV and IV components of venous vessels, regardless of the vessel size (see Fig. 10). Spin echo refocuses the dephasing effect around large vessels, and thus the spin-echo BOLD image contains the EV effect of vessels with time-irreversible diffusion effect (i.e., small-size vessel) and the IV component of all sizes of vessels. It is important to differentiate parenchyma signals (see a green rectangular box) from large vessel signals because the venous vasculature including large draining veins can be distant from the site of elevated neuronal activity (see also Fig. 10)^{32, 47-50}. Dilution by blood draining from “inactive” areas should ultimately diminish this non-specific draining-vein effect and thus limit its extent; however, before this occurs, substantial less-specific “activation” can be generated⁵¹. Therefore, it is important to minimize draining-vein signals from both intravascular and extravascular contributions for high-resolution studies.

The IV component can be reduced by setting an echo time of $>3T_2^*$ or $3T_2$ of blood. Thus, at ultrahigh fields, the IV component can be significantly reduced because venous blood T_2^*/T_2 decreases faster than tissue T_2^*/T_2 when magnetic field increases. The IV contribution to the BOLD responses can be examined using bipolar gradients⁵². These gradients induce velocity-dependent phase shifts in the presence of flow and consequently suppress signals from blood because of inhomogeneous velocities within a vessel and the presence of blood vessels of different orientations within a voxel. Based on bipolar studies, the BOLD fMRI signals at 1.5 T

originate predominantly from the IV component (70-90%)^{44, 53, 54}, while those at 7T and 9.4T come predominantly from the EV component (see Fig. 11)^{41, 55}. When bipolar gradients increased to $> 400 \text{ s/mm}^2$, relative percent BOLD signal change maintained constant, even though signal intensity decreased. With relatively high sensitivity of spin-echo BOLD at high fields, high-resolution functional maps can be obtained from human brain at 7T (see Fig. 11).

After removing the IV component in the BOLD signal, the EV component remains. In gradient-echo BOLD fMRI, the EV effect around large vessels is linearly dependent on magnetic field, while the EV effect around small vessels is supra-linearly dependent on magnetic field. Even at 9.4T, the EV effect around large vessels is significant. In spin-echo BOLD fMRI, the EV effect around small vessels is supra-linearly dependent on magnetic field, while that around large vessels is minimized. Thus, the spin-echo technique is more specific to parenchyma than gradient-echo BOLD fMRI. However, since the dephasing effect around vessels is refocused, the sensitivity of spin-echo BOLD signal is significantly reduced. For example, $\Delta R_2/\Delta R_2^*$ is 0.3 – 0.4 at 1.5T^{56, 57}, and also at 9.4T²¹. Even if respective optimized echo times are used for gradient-echo and spin-echo BOLD fMRI, the gradient-echo BOLD technique provides the higher signal change even at 9.4T. For most applications of the BOLD technique, the gradient-echo BOLD technique is the choice of tools because of high sensitivity even if its spatial specificity compromises.

1.4. Contrast-to-noise Ratio

Important consideration of fMRI is contrast-to-noise ratio (neural activity-induced signal change relative to signal fluctuation). Increase of neural activity-induced MRI signal and

decrease of noise are important aspects for high-resolution fMRI. Neural activity-induced signal is dependent on both image contrast and imaging techniques used for fMRI. In the T_2^* -based measurements, the signal change induced by neural activity (ΔS) can be described by

$$\Delta S = \Delta S_{\text{cont}} \left(e^{-\Delta R_2^* \text{TE}} - 1 \right) \quad [9]$$

where Δ is the fraction of a voxel that is active, S_{cont} is the signal intensity during the control period, TE is the echo time, and ΔR_2^* is the change in the apparent transverse relaxation rate in the active partial volume. Signal change is maximal when a gradient echo time is set to T_2^* of tissue at resting conditions. When spin echo imaging techniques are used, ΔR_2^* is replaced by ΔR_2 . ΔR_2^* is equivalent to $\Delta R_2 + \Delta R_2'$ where $\Delta R_2'$ is the relaxation rate induced by local inhomogeneous magnetic fields. ΔS for spin-echo BOLD fMRI will be maximal by setting TE of T_2 of tissue. In CBF-based techniques, $\text{TE} \Delta R_2^*$ is substituted by $\text{TI} \Delta R_1^*$ where TI is the spin labeling time (i.e., the inversion time for pulsed labeling methods), and ΔR_1^* is the change in the apparent longitudinal relaxation rate. ΔS is maximized by setting TI of T_1 of tissue. In any techniques, contribution of large vessels increases ΔS . Depending on constraints of spatial specificity for each measurement, the technique with the highest ΔS should be chosen. Since contribution of small intracortical veins is likely localized within 1.5 mm to the site of activation⁵⁸, contribution of small veins can improve SNR for supramillimeter spatial resolution. In typical fMRI studies with supramillimeter spatial resolution, the removal of only large surface arteries and veins may be necessary.

Sources of noise include random white noise, physiological fluctuations, bulk head motion, and system instability if exists. Random noise is independent between voxels, while other noise sources may be coherent among voxels, resulting in spatial and temporal correlation.

In fMRI, coherent noises are the major source of signal fluctuation. Bulk head motion can be eliminated by head holders. Physiological motion, which is mainly due to respiration and cardiac pulsation, can be minimized by gating data acquisition and/or reduced by post-processing^{59, 60}.

1.5. Spatial and Temporal Resolution of fMRI

1.5.1. Spatial Resolution

Spatial resolution of high-resolution fMRI is dependent on SNR and intrinsic hemodynamic response. The intrinsic limit of spatial specificity of hemodynamic-based fMRI can be dependent on how finely CBF is regulated. It has been suggested, based on optical imaging studies, that CBF regulation is widespread beyond neuronally active areas⁶¹. However, recent studies suggest that intrinsic CBF changes are specific to sub-millimeter functional domains³¹. Especially, the highest CBF change was observed in the middle of the rat somatosensory cortex, cortical layer IV, not at the surface of the cortex during somatosensory stimulation^{21, 62}. This observation is consistent with invasive 2-DG and ¹⁴C-iodoantipyrine autoradiographic studies in the barrel cortex⁶³. To further examine the specificity of CBF response, the perfusion-based FAIR technique has been utilized²³. From this study, we found that CBF is regulated to sub-millimeter columnar and laminar-specific functional domains^{21, 31}. Among the available hemodynamic fMRI approaches, the CBF-based signal is the most specific to neuronal active sites because most of signals originate from tissue and capillaries. Tissue-specific BOLD signal without large vessel contribution will have a similar spatial specificity to the CBF-weighted signal²¹.

1.5.2. Temporal Resolution

Since hemodynamic responses are sluggish, it is difficult to obtain very high temporal resolution even if images can be obtained rapidly. Typically, hemodynamic signal changes are observed at 1-2 seconds after onset of neural stimulation and reaches maximum at 4 – 8 seconds (see Fig. 12). The exact time of neural activity from hemodynamic responses can not be easily obtained because hemodynamic response varies depending on vascular structures (see Fig 12). The important question is to determine sequential neural activities of different cortical regions or pixels. If the hemodynamic response times in all regions and in all subjects were the same, neuronal activities could be directly inferred from fMRI time courses. However, this may not be true in all regions and in all subjects (see Fig. 12), and thus differences in fMRI time courses may be simply related to intrinsic hemodynamic response time differences, hampering temporal studies. Thus, temporal resolution of fMRI is limited. Alternative approaches to overcome these problems have been proposed. To separate intrinsic hemodynamic differences from neural activity differences, a time-resolved event-related fMRI technique can be utilized ⁶⁴⁻⁶⁷. The idea is to examine how fMRI parameters vary with behavioral correlates and thus requires multiple behavioral outcome measures. Subsequently, temporal characteristics of fMRI responses can be correlated with behavioral data such as response time. Differences in the underlying temporal behavior of neuronal activity can be distinguished from hemodynamic response time variations between subjects and brain areas (see a review article ⁶⁸). This approach allows the experimenter to obtain higher temporal resolution. Dynamic fMRI studies can be feasible using standard gradient-echo BOLD fMRI.

1.6. Conclusions

Advancement of imaging technologies allows detections of various vascular physiological parameters induced by neural activity. Fortunately, tissue-based hemodynamic response is specific to neuronal active sites. Thus, spatial resolution of fMRI can be achieved up to on an order of a column, allowing mapping column- and layer-specific neural activities. Since hemodynamic response is slow, its temporal resolution can not be reached at a level of neural activity time scale easily. By using an approach with multiple experiments with different stimulus intervals or durations, temporal resolution can be improved up to on the order of 100 milliseconds.

Acknowledgements

Supported by the National Institutes of Health (NS38295, NS40719, NS44589, MH57180), and the McKnight Foundation Neuroscience Endowment.

1.7. References

1. Roy CS, Sherrington CS. On the regulation of blood supply of the brain. *J Physiol* 1890; 1:85-108.
2. Raichle ME. Circulatory and metabolic correlates of brain function in normal humans. *Handbook of Physiology-The Nervous System*. Vol. Vol V. Bethesda: American Physiological Society, 1987:643-674.
3. Fox PT, Raichle ME. Focal physiological uncoupling of cerebral blood flow and oxidative metabolism during somatosensory stimulation in human subjects. *Proc Natl Acad Sci USA* 1986; **83**:1140-1144.
4. Fox PT, Raichle ME, Mintun MA, Dence C. Nonoxidative glucose consumption during focal physiologic neural activity. *Science* 1988; 241:462-464.
5. Ogawa S, Lee T-M, Nayak AS, Glynn P. Oxygenation-sensitive contrast in magnetic resonance image of rodent brain at high magnetic fields. *Magn Reson Med* 1990; 14:68-78.
6. Ogawa S, Lee T-M, Kay AR, Tank DW. Brain Magnetic Resonance Imaging with Contrast Dependent on Blood Oxygenation. *Proc Natl Acad Sci USA* 1990; 87:9868-9872.
7. Ogawa S, Lee TM. Magnetic Resonance Imaging of Blood Vessels at High Fields: in Vivo and in Vitro Measurements and Image Simulation. *Magn Reson Med* 1990; 16:9-18.
8. Pauling L, Coryell CD. The magnetic properties and structure of hemoglobin, oxyhemoglobin and carbonmonoxyhemoglobin. *Proc Natl Acad Sci USA* 1936; 22:210-216.

9. Thulborn KR, Waterton JC, Matthews PM, Radda GK. Oxygenation Dependence of the Transverse Relaxation Time of Water Protons in Whole Blood at High Field. *Biochem Biophys Acta* 1982; **714**:265-270.
10. Ogawa S, Tank DW, Menon R, et al. Intrinsic Signal Changes Accompanying Sensory Stimulation: Functional Brain Mapping with Magnetic Resonance Imaging. *Proc Natl Acad Sci USA* 1992; 89:5951-5955.
11. Kwong KK, Belliveau JW, Chesler DA, et al. Dynamic Magnetic Resonance Imaging of Human Brain Activity during Primary Sensory Stimulation. *Proc Natl Acad Sci USA* 1992; **89**:5675-5679.
12. Bandettini PA, Wong EC, Hinks RS, Rikofsky RS, Hyde JS. Time course EPI of human brain function during task activation. *Magn Reson Med* 1992; 25:390-397.
13. Ogawa S, Menon RS, Kim S-G, Ugurbil K. On the characteristics of functional magnetic resonance imaging of the brain. *Annu Rev Biophys Biomol Struct* 1998; 27:447-474.
14. Grubb RL, Raichle ME, Eichling JO, Ter-Pogossian MM. The effects of changes in PaCO₂ on cerebral blood volume, blood flow, and vascular mean transit time. *Stroke* 1974; 5:630-639.
15. Lee S-P, Duong T, Yang G, Iadecola C, Kim S-G. Relative changes of cerebral arterial and venous blood volumes during increased cerebral blood flow: Implications for BOLD fMRI. *Magn Reson Med* 2001; 45:791-800.
16. Ito H, Takahashi K, Hatazawa J, Kim S-G, Kanno I. Changes in human regional cerebral blood flow and cerebral blood volume during visual stimulation measured by positron emission tomography. *J Cereb Blood Flow Metab* 2001; 21:608-612.

17. Ogawa S, Menon RS, Tank DW, et al. Functional Brain Mapping by Blood Oxygenation Level-Dependent Contrast Magnetic Resonance Imaging. *Biophys J* 1993; 64:800-812.
18. Hoge RD, Atkinson J, Gill B, Crelier GR, Marrett S, G.B. P. Linear coupling between cerebral blood flow and oxygen consumption in activated human cortex. *Proc Natl Acad Sci* 1999; 96:9403-9408.
19. Kim S-G, Rostrup E, Larsson HBW, Ogawa S, Paulson OB. Simultaneous measurements of CBF and CMRO₂ changes by fMRI: Significant increase of oxygen consumption rate during visual stimulation. *Magn Reson Med* 1999; 41:1152-1161.
20. Silva A, Lee S-P, Yang C, Iadecola C, Kim S-G. Simultaneous BOLD and perfusion functional MRI during forepaw stimulation in rats. *J Cereb Blood Flow Metab* 1999; 19:871-879.
21. Lee S-P, Silva AC, Kim S-G. Comparison of Diffusion-weighted High-Resolution CBF and Spin-Echo BOLD fMRI at 9.4 T. *Magn Reson Med* 2002; 47:736-741.
22. Detre JA, Leigh JS, Williams DS, Koretsky AP. Perfusion imaging. *Magn Reson Med* 1992; 23:37-45.
23. Kim S-G. Quantification of relative cerebral blood flow change by flow-sensitive alternating inversion recovery (FAIR) technique: application to functional mapping. *Magn Reson Med* 1995; 34:293-301.
24. Kwong KK, Chesler DA, Weisskoff RM, et al. MR perfusion studies with T1-weighted echo planar imaging. *Magn Reson Med* 1995; 34:878-887.
25. Schwarzbauer C, Morrissey S, Haase A. Quantitative magnetic resonance imaging of perfusion using magnetic labeling of water proton spins within the detection slice. *Magn Reson Med* 1996; 35:540-546.

26. Edelman RR, Siewert B, Darby DG, et al. Qualitative mapping of cerebral blood flow and functional localization with echo-planar MR imaging and signal targeting with alternating radio frequency. *Radiology* 1994; 192:513-520.
27. Helpert J, Branch C, Yongbi M, Huong N. Perfusion imaging by un-inverted flow-sensitive alternating inversion recovery (UNFAIR). *Magn Reson Imaging* 1997; 15:135-139.
28. Wong E, Buxton R, Frank L. Quantitative imaging of perfusion using a single subtraction (QUIPSS and QUIPSS II). *Magn Reson Med* 1998; 39:702-708.
29. Zaini MR, Strother SC, Andersen JR, et al. Comparison of matched BOLD and FAIR 4.0T-fMRI with [^{15}O]water PET brain volumes. *Medical Physics* 1999; 26:1559-1567.
30. Lowel S, Freeman B, Singer W. Topographic organization of the orientation column system in large flat-mounts of the cat visual cortex: a 2-deoxyglucose study. *Exp Brain Res* 1988; 71:33-46.
31. Duong TQ, Kim D-S, Ugurbil K, Kim S-G. Localized cerebral blood flow response at submillimeter columnar resolution. *Proc. Natl. Acad. Sci. USA* 2001; 98:10904-10909.
32. Duong TQ, Kim D-S, Ugurbil K, Kim S-G. Spatio-temporal Dynamics of the BOLD fMRI Signals: Toward Mapping Submillimeter Columnar Structures Using the Early Negative Response. *Magn Reson Med* 2000; 44:231-242.
33. Kim D-S, Duong TQ, Kim S-G. High-resolution mapping of iso-orientation columns by fMRI. *Nature Neurosci* 2000; 3:164-169.
34. Ye FQ, Mattay VS, Jezzard P, Frank JA, Weinberger DR, McLaughlin AC. Correction for vascular artifacts in cerebral blood flow values by using arterial spin tagging techniques. *Magn. Reson. Med.* 1997; 37:226-235.

35. Kim S-G, Tsekos NV. Perfusion imaging by a flow-sensitive alternating inversion recovery (FAIR) technique: Application to functional mapping. *Magn Reson Med* 1997; 37:425-435.
36. Buxton R, Frank L, Wong E, Siewert B, Warach S, Edelman R. A general kinetic model for quantitative perfusion imaging with arterial spin labeling. *Magn. Reson. Med.* 1998; 40:383-396.
37. Weisskoff RM, Zuo CS, Boxerman JL, Rosen BR. Microscopic susceptibility variation and transverse relaxation: Theory and Experiment. *Magn Reson in Med* 1994; 31:601-610.
38. Wright GA, Hu BS, Macovski A. Estimating oxygen saturation of blood in vivo with MR imaging at 1.5 T. *J Magn Reson Imag* 1991; 1:275-283.
39. Ogawa S, Lee TM, Barrere B. Sensitivity of magnetic resonance image signals of a rat brain to changes in the cerebral venous blood oxygenation. *Magn Reson Med* 1993; 29:205-210.
40. Yacoub E, Shmuel A, Pfeuffer J, et al. Imaging brain function in humans at 7 Tesla. *Magn Reson Med* 2001; 45:588-594.
41. Lee S-P, Silva AC, Ugurbil K, Kim S-G. Diffusion-weighted spin-echo fMRI at 9.4 T: microvascular/tissue contribution to BOLD signal change. *Magn Reson Med* 1999; 42:919-928.
42. Breger RK, Rimm AA, Fischer ME, Papke RA, Haughten VM. T_1 and T_2 Measurements on a 1.5 Tesla Commercial Imager. *Radiology* 1989; 171:273-276.

43. Haacke E, Lai S, Yablonskiy D, Lin W. In vivo validation of the BOLD mechanism: A review of signal changes in gradient echo functional MRI in the presence of flow. *Int J Imaging Systems Technology* 1995; 6:153-163.
44. Boxerman JL, Bandettini PA, Kwong KK, et al. The intravascular contribution to fMRI signal change: Monte Carlo modeling and diffusion-weighted studies in vivo. *Magn Reson Med* 1995; 34:4-10.
45. Kennan RP, Zhong J, Gore JC. Intravascular susceptibility contrast mechanisms in tissues. *Magn Reson Med* 1994; 31:9-21.
46. Bandettini PA, Wong EC. Effects of biophysical and physiologic parameters on brain activation-induced $R2^*$ and $R2$ changes: Simulations using a deterministic diffusion model. *Int J Imaging Systems Technology* 1995; 6:133-152.
47. Lai S, Hopkins AL, Haacke EM, et al. Identification of vascular structures as a major source of signal contrast in high resolution 2D and 3D functional activation imaging of the motor cortex at 1.5T: preliminary results. *Magn Reson Med* 1993; 30:387-392.
48. Menon RS, Ogawa S, Tank DW, Ugurbil K. 4 Tesla Gradient Recalled Echo Characteristics of Photic Stimulation-Induced Signal Changes in the Human Primary Visual Cortex. *Magn Reson Med* 1993; **30**:380-386.
49. Kim S-G, Hendrich K, Hu X, Merkle H, Ugurbil K. Potential pitfalls of functional MRI using conventional gradient-recalled echo techniques. *NMR in Biomed* 1994; 7:69-74.
50. Frahm J, Merboldt K-D, Hancic W, Kleinschmidt A, Boecker H. Brain or vein-oxygenation or flow? On signal physiology in functional MRI of human brain activation. *NMR in Biomed* 1994; 7:45-53.

51. Kim S-G, Ugurbil K. Functional magnetic resonance imaging of the human brain. *J Neurosci Methods* 1997; 74:229-243.
52. Stejskal EO, Tanner JE. Spin diffusion measurements: Spin echoes in the presence of a time-dependent field gradient. *J Chem Physics* 1965; 42:288-292.
53. Song AW, Wong EC, Tan SG, Hyde JS. Diffusion-weighted fMRI at 1.5T. *Magn Reson Med* 1996; 35:155-158.
54. Zhong J, Kennan RP, Fulbright RK, Gore JC. Quantification of intravascular and extravascular contributions to BOLD. *Magnetic Resonance in Medicine* 1998; 40:526-36.
55. Duong TQ, Yacoub E, Adriany G, Hu X, Ugurbil K, Kim S-G. Microvascular BOLD Contribution at 4 and 7 Tesla in the Human Brain: Diffusion-weighted, Gradient-Echo and Spin-Echo fMRI. *Mag Reson Med* 2002:accepted.
56. Bandettini PA, Wong EC, Jesmanowicz A, Hinks RS, Hyde JS. Spin-echo and gradient-echo EPI of human brain activation using BOLD contrast: a comparative study at 1.5 T. *NMR in Biomed.* 1994; 7:12-20.
57. Lowe M, Lurito J, Mattews V, Phillips M, Hutchins G. Quantitative comparison of functional contrast from BOLD-weighted spin-echo and gradient-echo echoplanar imaging at 1.5 Tesla and H215O PET in the whole brain. *J Cereb Blood Flow Metabolism* 2000; 20:1331-1340.
58. Duvernoy H, Delon S, Vannson J. Cortical blood vessels of the human brain. *Brain Res Brain* 1981; 7:519-579.
59. Hu X, Kim S-G. Reduction of signal fluctuations in functional MRI using navigator echos. *Magn Reson Med* 1994; 31:495-503.

60. Hu X, Le TH, Parrish T, Erhard P. Retrospective estimation and compensation of physiological fluctuation in functional MRI. *Magn Reson Med* 1995; 34:210-221.
61. Malonek D, Grinvald A. Interactions between electrical activity and cortical microcirculation revealed by imaging spectroscopy: Implication for functional brain mapping. *Science* 1996; 272:551-554.
62. Duong TQ, Silva AC, Lee S-P, Kim S-G. Functional MRI of Calcium-Dependent Synaptic Activity: Cross Correlation with CBF and BOLD measurements. *Magn Reson Med* 2000; 43:383-392.
63. Woolsey TA, Rovainen CM, Cox SB, et al. Neuronal units linked to microvascular modules in cerebral cortex: Response elements for imaging the brain. *Cereb Cortex* 1996; 6:647-660.
64. Kim S-G, Richter W, Ugurbil K. Limitations of temporal resolution in fMRI. *Magn Reson Med* 1997; 37:631-636.
65. Richter W, Andersen PM, Georgopoulos AP, Kim S-G. Sequential activity in human motor areas during a delayed cued movement task studied by time-resolved fMRI. *NeuroReport* 1997; 8:1257-1261.
66. Richter W, Ugurbil K, Georgopoulos AP, Kim S-G. Time-resolved fMRI of mental rotation. *NeuroReport* 1997; 8:3697-3702.
67. Richter W, Somorijai R, Summers R, et al. Motor area activity during mental rotation studied by time-resolved single-trial fMRI. *J Cogn Neurosci* 2000; 12:310-320.
68. Menon R, Kim S-G. Spatial and temporal limits in cognitive neuroimaging with fMRI. *Trends Cogn. Sci.* 1999; 3:207-215.

69. Duong TQ, Kim S-G. In vivo MR measurements of regional arterial and venous blood volume fractions in intact rat brain. *Magn Reson Med* 2000; 43:393-402.
70. Kim S-G, Tsekos NV, Ashe J. Multi-slice perfusion-based functional MRI using the FAIR technique: Comparison of CBF and BOLD effects. *NMR in Biomedicine* 1997; 10:191-196.
71. Bandettini PA. The temporal resolution of Functional MRI. In: Moonen CTW, Bandettini PA, eds. *Functional MRI*. New York: Springer, 1999:205-220.
72. Duong TQ, Yacoub E, Adriany G, et al. High-Resolution, Spin-echo BOLD and CBF fMRI at 4 and 7 T. *Mag Reson Med* 2002:in press.

Figure captions

Figure 1. A schematic of fMRI signal changes induced by stimulation. Task/stimulation increases neural activity, and increase metabolic (cerebral metabolic rate of oxygen) and vascular responses (cerebral blood flow and volume). Increase in CBF enhances venous oxygenation level, while increase in CMRO₂ decreases venous oxygenation level. Since an increase in CBF exceeds an increase in CMRO₂, venous oxygenation level increases. These vascular parameter changes will modulate biophysical parameters. Increases in CBF and CBV increase R_1 and R_2 , respectively, while decrease in dHb contents reduces R_2 . Changes in biophysical parameters affect MRI signal changes.

Figure 2. Relationship between CBF and CBV in rat brain ¹⁵. CBF and CBV were measured using arterial spin labeling and ¹⁹F NMR after injection of blood substitute perfluorocarbons during hypercapnia. CBV values were normalized with the CBV value at normocapnia (CBF = 58 ml/100 g/min). (a) Relationship between CBF and total CBV. The change in total rCBV was linearly correlated with the change in rCBF in a CBF range of 50 – 130 ml/100 g/min ($rCBV(total) / rCBF = 0.31$). (b) Relationship between CBF and arterial/venous CBV. Arterial and venous CBV can be separated by using diffusion-weighted ¹⁹F NMR ⁶⁹. The contribution of venous CBV changes to total CBV change is ~36%.

Figure 3. Hypothetical longitudinal magnetization with and without inflow effect after application of an inversion pulse. Inflow effects relax spins faster.

Figure 4. CBF-weighted functional image during left finger movements ⁷⁰. To obtain the perfusion contrast, flow direction (indicated by an up-arrow) has to be considered. Thus, 5 mm-thick transverse planes were selected for CBF-based fMRI studies. The background image was perfusion-weighted; higher signal areas have higher inflow rates. Functional activity areas are located at gray matter in the contralateral primary motor cortex indicated by a red arrow. Interestingly, no large signal changes were observed at the edge of the brain, which was often seen in conventional BOLD functional maps.

Figure 5. Application of the CBF-based (FAIR) fMRI technique to isoflurane-anesthetized cat's orientation column mapping ³¹. Moving gratings with black and white rectangular single-orientation bars were used for visual stimulation. Unlike the conventional BOLD technique, CBF-weighted fMRI is specific to tissue, not draining vessels. More importantly, active clusters are irregular and column-like based on the size of clusters and the interval between clusters. Also, single-condition functional regions activated by two orthogonal orientation stimuli are complementary. Scale bar = 1 mm; Color vertical bar = t value. Time course of activation area is shown. Boxes underneath the time course indicate 1-min long stimulation periods. Typical CBF change induced by visual stimulation ranges between 15 and 50%.

Figure 6. Diagram of a blood vessel and the parameters that determine the susceptibility effect induced by deoxyhemoglobin irons in red blood cells at a distance r from the center of a vessel. The vessel with a radius of a is oriented at angle θ from the main magnetic field B_0 . θ is the angle between r and plane defined by B_0 and the vessel axis.

Figure 7. Spin-echo and gradient-echo image of a capillary filled with blood with deoxyhemoglobin⁷. Two different orientations were used. When vessel orientation is parallel to B_0 , no signal change outside the capillary was observed. But, when vessel is orthogonal to B_0 , gradient-echo signal change outside the capillary was detected.

Figure 8. Extravascular dephasing effects from a 3 μ m radius capillary and a 30 μ m radius venule. Magnitude of dephasing effect (dashed decay lines from vessels) is shown as a function of distance. Hypothetical displacement of a water molecule is shown. Refocusing RF pulse in the spin-echo sequence can not refocus dephasing effects around a small vessel because of dynamic averaging, while it can refocus static dephasing (shown in averaged phases in circles).

Figure 9. R_2^* and R_2 changes as a function of vessel radius^{17,46}. Monte Carlo simulation was performed to calculate R_2^* change induced by three frequency shifts¹⁷.

Figure 10. Intravascular and extravascular signal contributions to perfusion and BOLD signals⁷¹. In perfusion-weighted images, the IV component of all arterial vessels (red color) and EV component (black) of capillaries will constitute. When spin-echo data collection is used, spins in large vessels will not be refocused, removing very large arteries contribution. Further removal can be achieved by using bipolar flow-crushing gradients. In BOLD images, IV (blue color) and EV (black) components of all sizes venous vessels will contribute when gradient-echo data collection is used. When spin-echo data collection is utilized, EV effect of large vessels can be minimized. Spatial heterogeneity of vascular distributions exists; in some pixels, large vessels are dominant, while some pixels contain mostly capillaries. When neural activity occurs at tissue

level, demarked by a green rectangle, only capillary-level signal change will locate the actual neural activity area. Containing large vessels will misleadingly deviate activation to non-specific vessel area.

Figure 11. Spin-echo BOLD based fMRI at 9.4T and 7T^{41, 72}. (top) An α -chloralase anesthetized rat was used for somatosensory forelimb stimulation. Color indicates a cross-correlation value. Localized activation is observed at the forelimb S1. fMRI time courses of spin-echo BOLD signal in the primary somatosensory region. To investigate the IV component, flow-crushing gradients (in a unit of b value) were used. The higher b value will result in the more reduction of the moving blood signal. If the IV component is significant, we expect a much lower BOLD signal change when a larger b value is used. However, we did not observe any reduction of relative BOLD signals, suggesting that spin-echo BOLD signal does not contain a significant IV component. Somatosensory stimulation was performed during image number 20 to 29. (bottom) High-resolution spin-echo BOLD image was obtained from human during visual stimulation at 7T. At high fields, sensitivity of SE BOLD signal is sufficient for high-resolution mapping of human brain. Spatial resolution is 1 mm x 1 mm x 2 mm.

Figure 12. Heterogeneity of hemodynamic responses⁷¹. Delay time of T_2^* -weighted fMRI signal changes was obtained in the motor cortical areas. 2-sec bilateral finger movements were performed at 3 T. Although average delay time is ~ 1 sec, there is a large variation in delay time shown in color map as well as histogram. In histogram and the delay map, relative hemodynamic delay time (not actual delay time) was calculated, which means average of all delay times of 0 sec.

Fig. 1

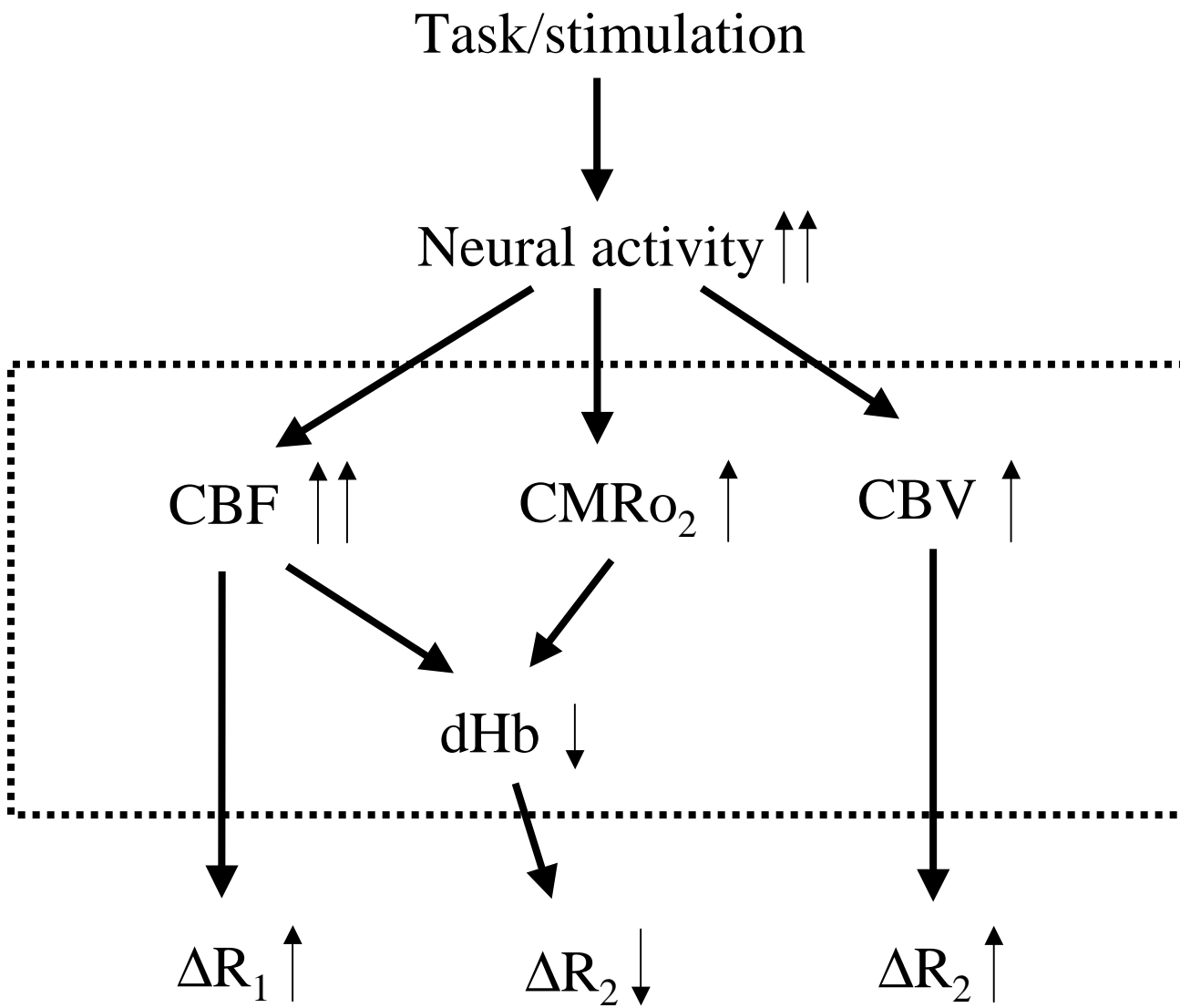


Fig. 2a

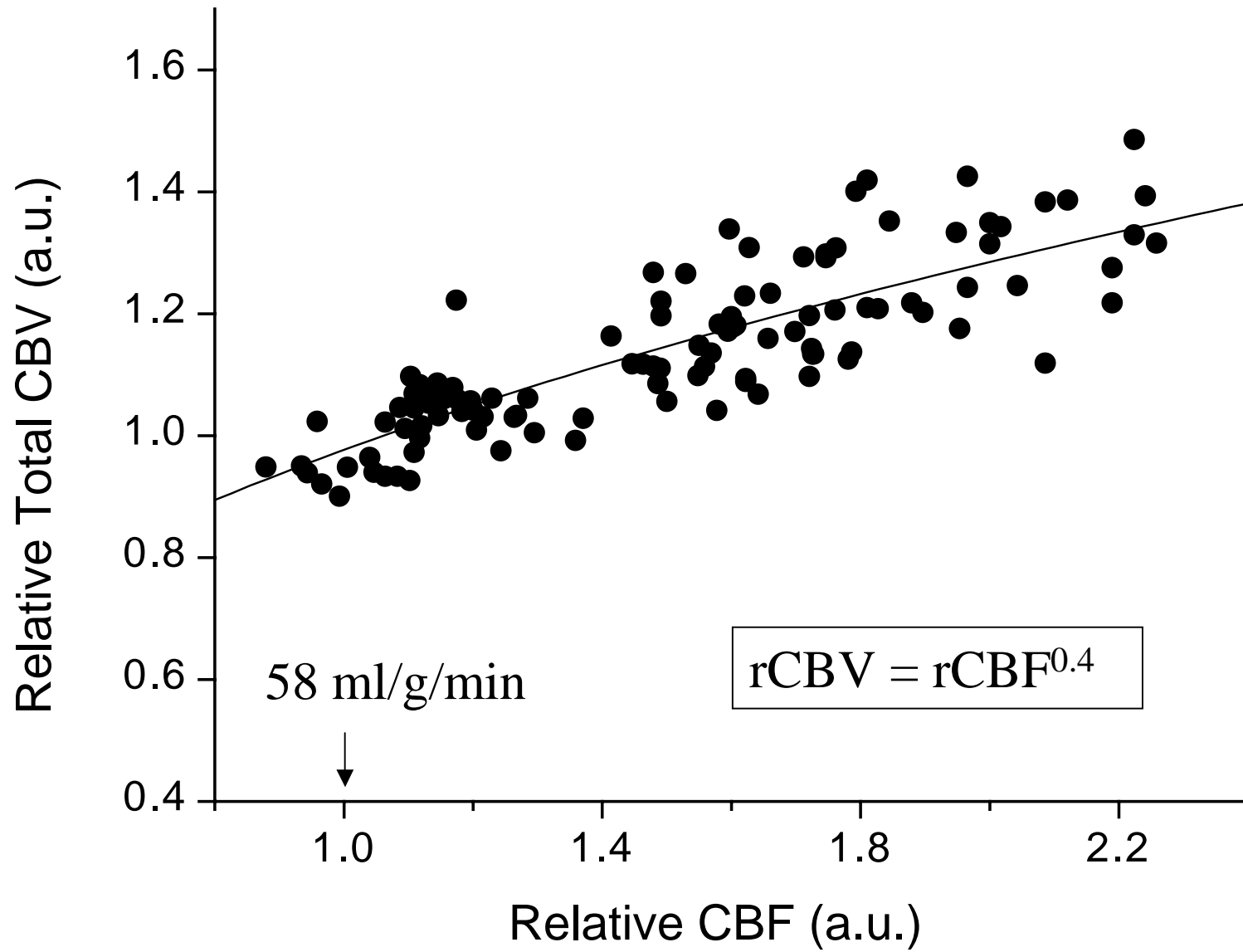


Fig. 2b

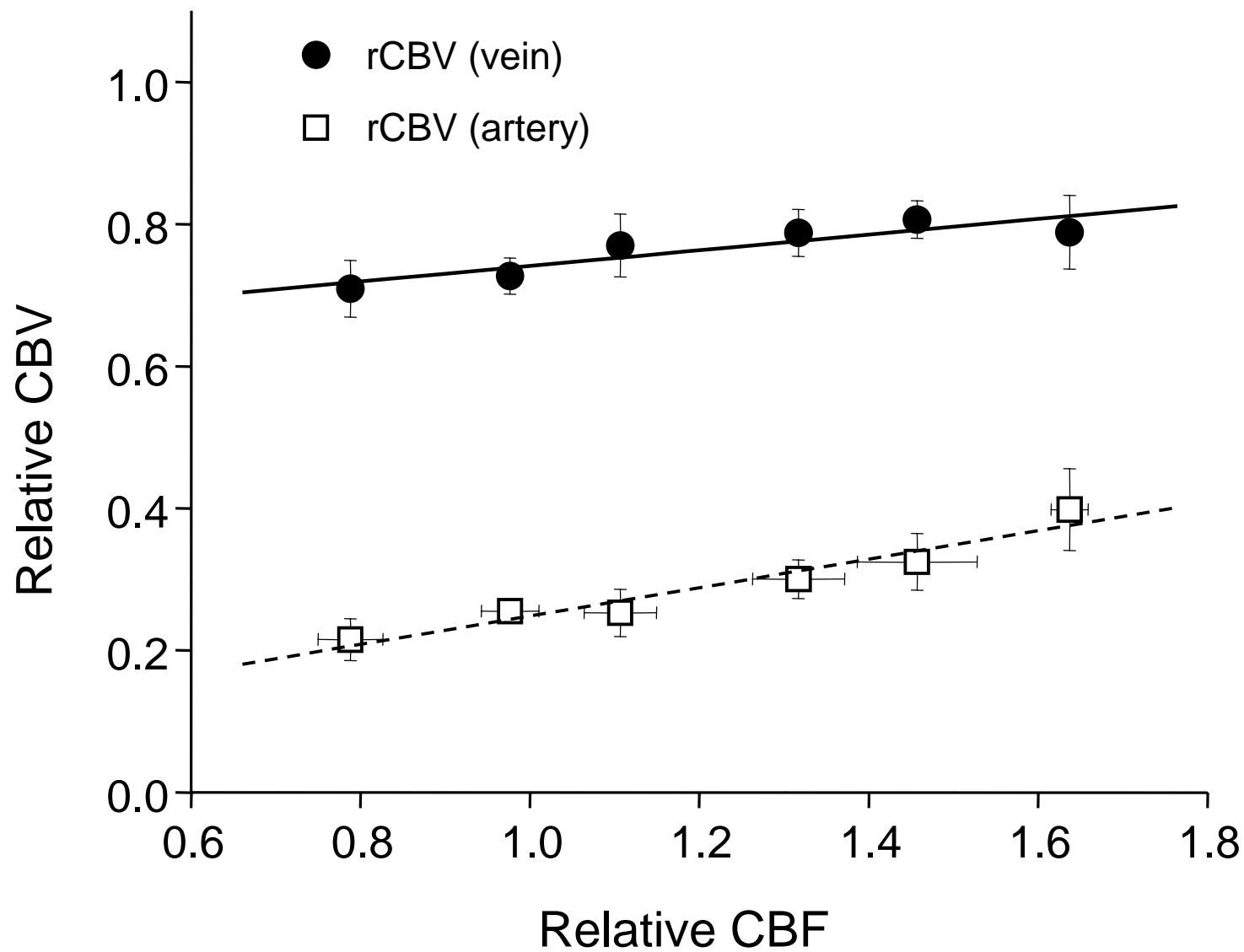


Fig. 3

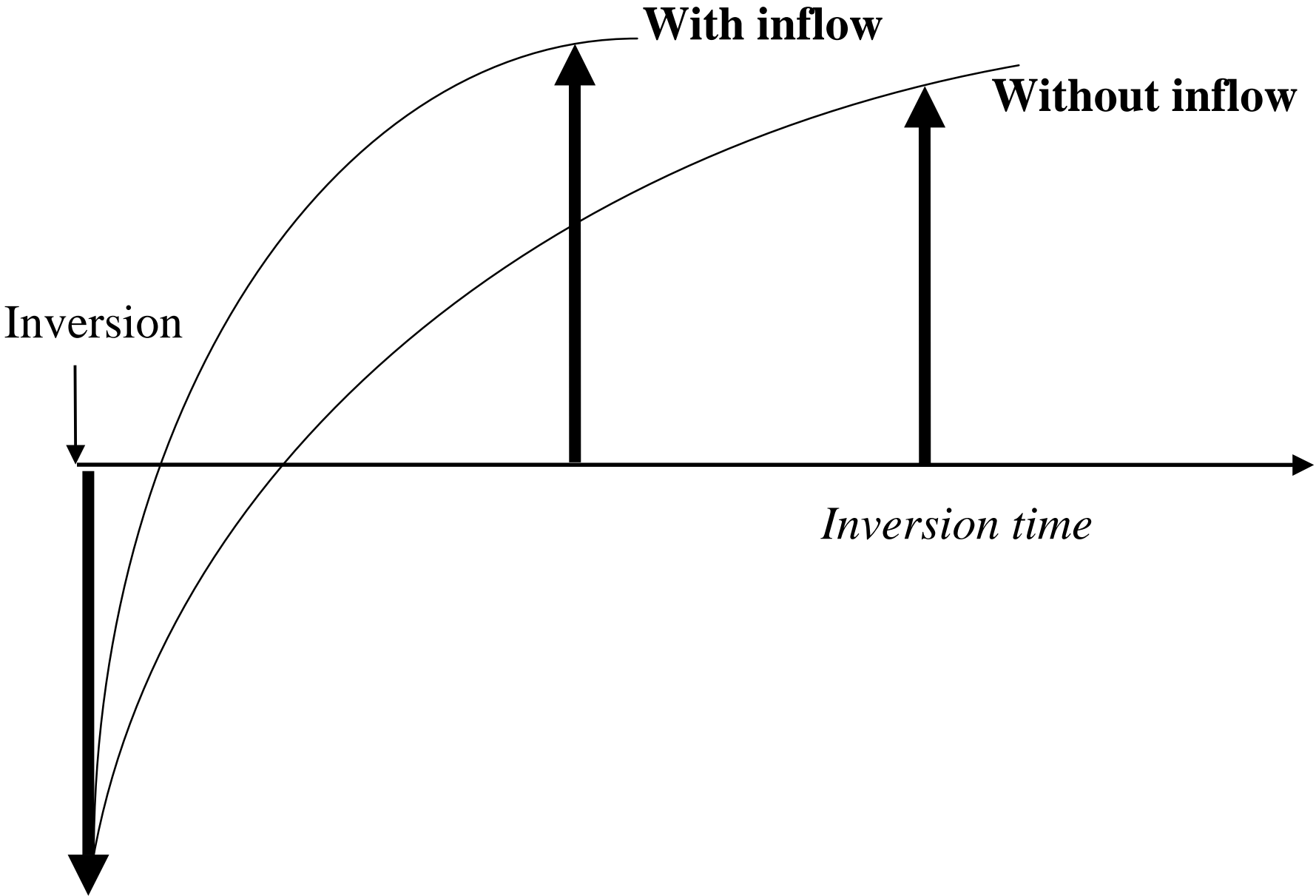


Fig. 4

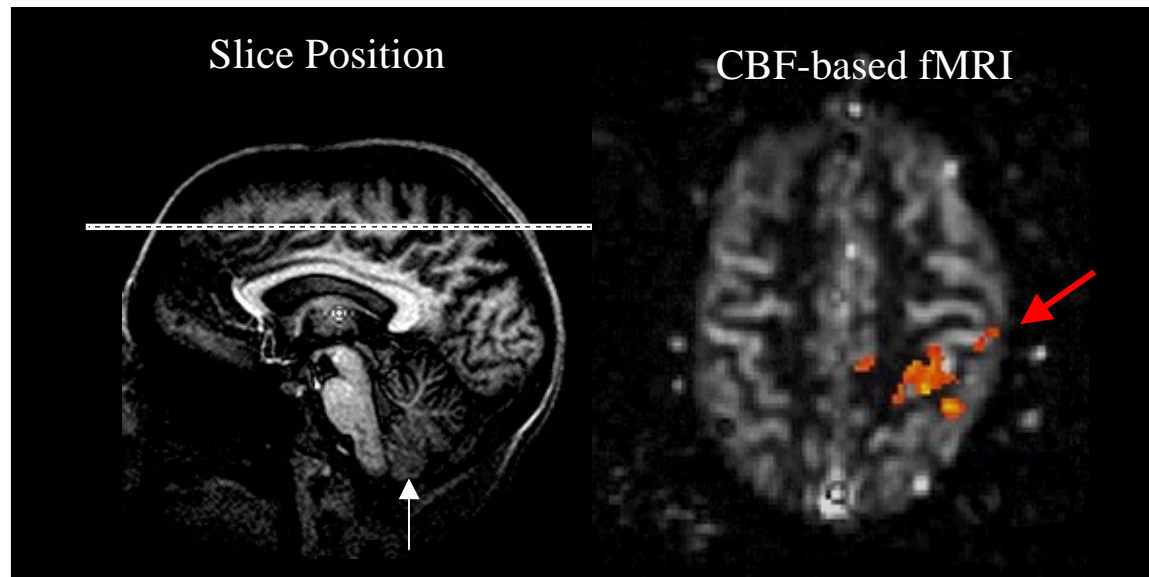


Fig. 5

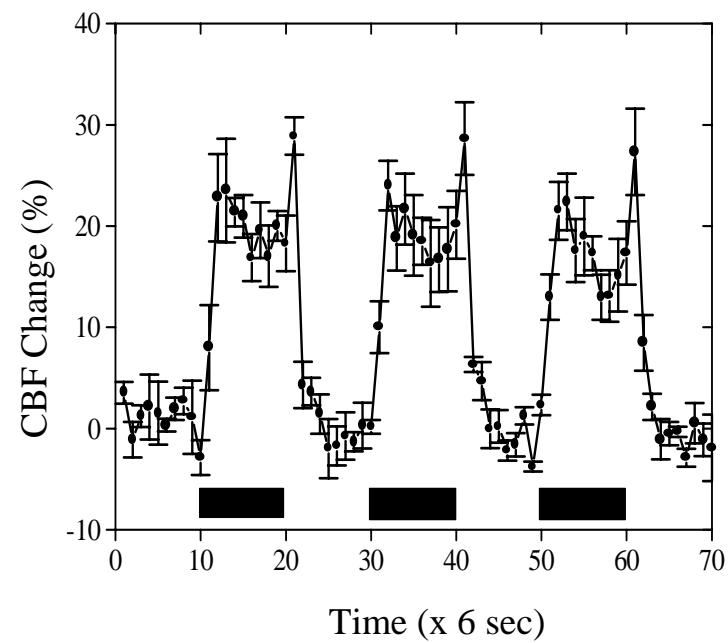
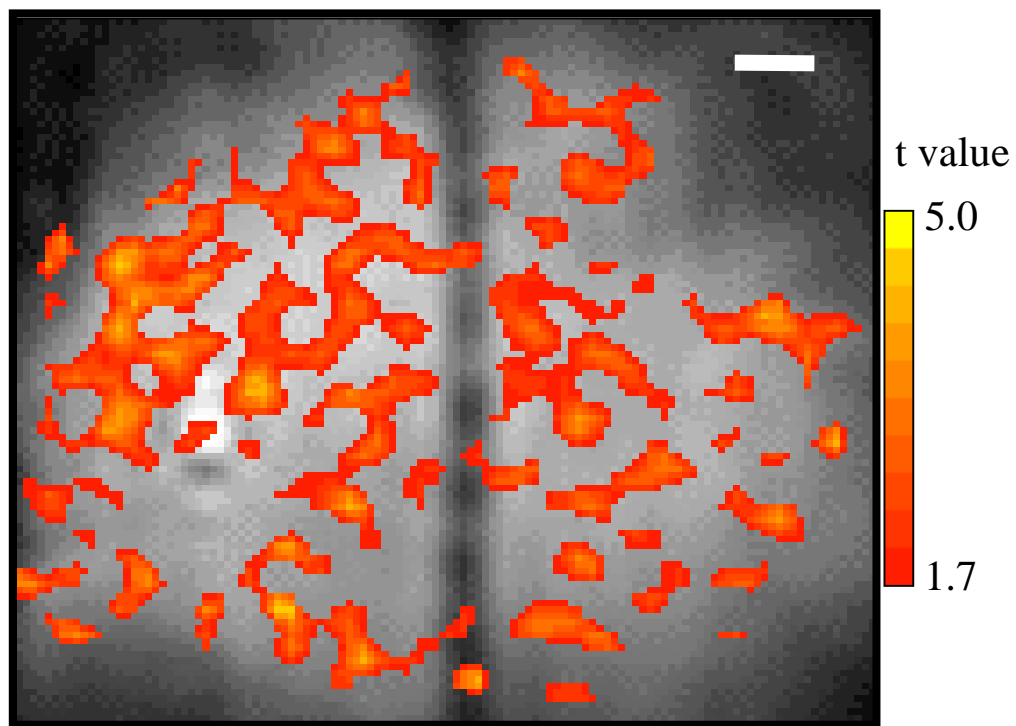
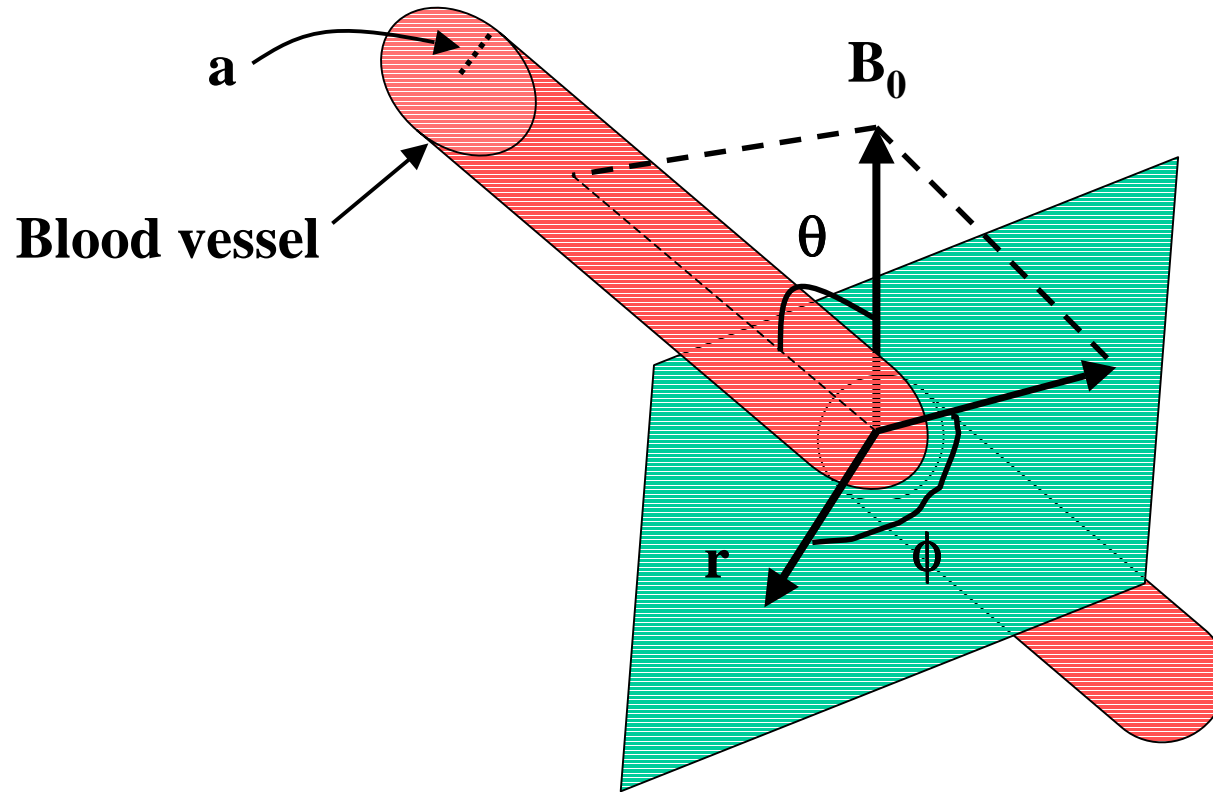


Fig. 6



$$\Delta\omega_{\text{in}} = 2\pi \Delta\chi_0 (1 - Y) \omega_0 (\cos^2\theta - 1/3)$$

$$\Delta\omega_{\text{out}} = 2\pi \Delta\chi_0 (1 - Y) \omega_0 (a/r)^2 (\sin^2\theta) (\cos 2\phi)$$

Fig. 7

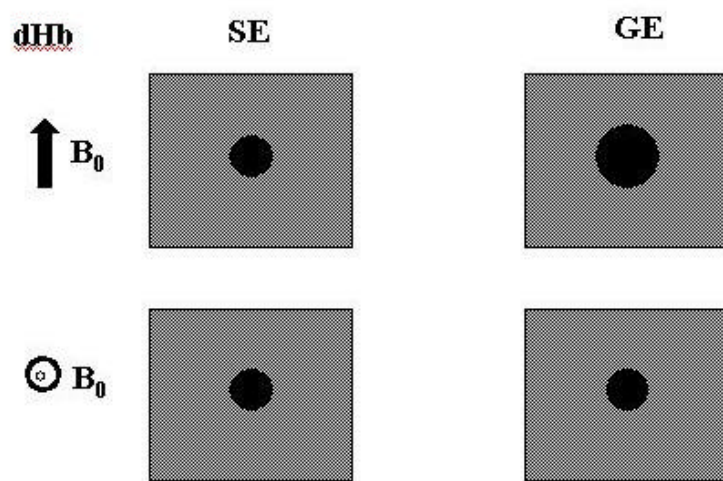


Fig. 8

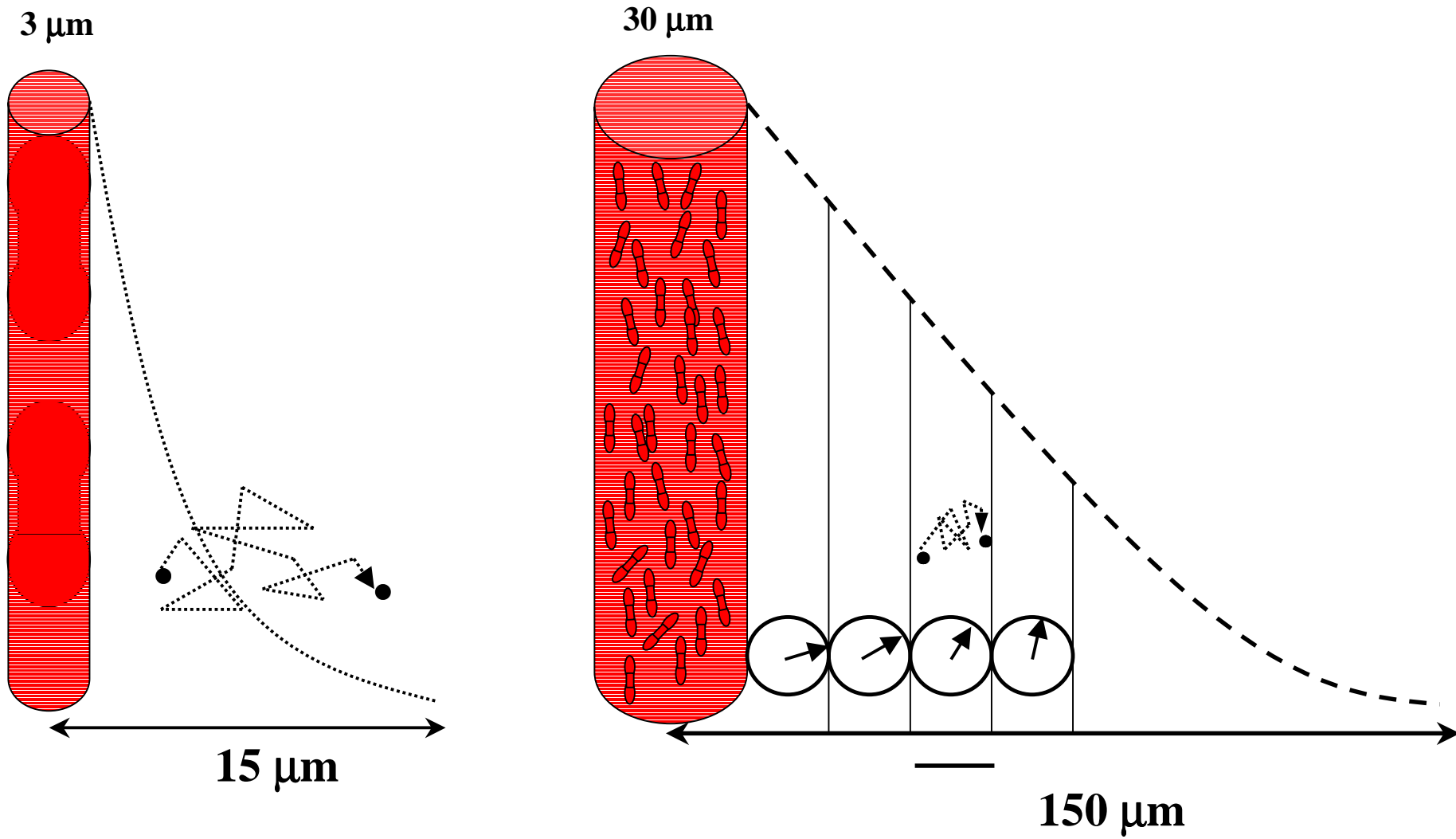
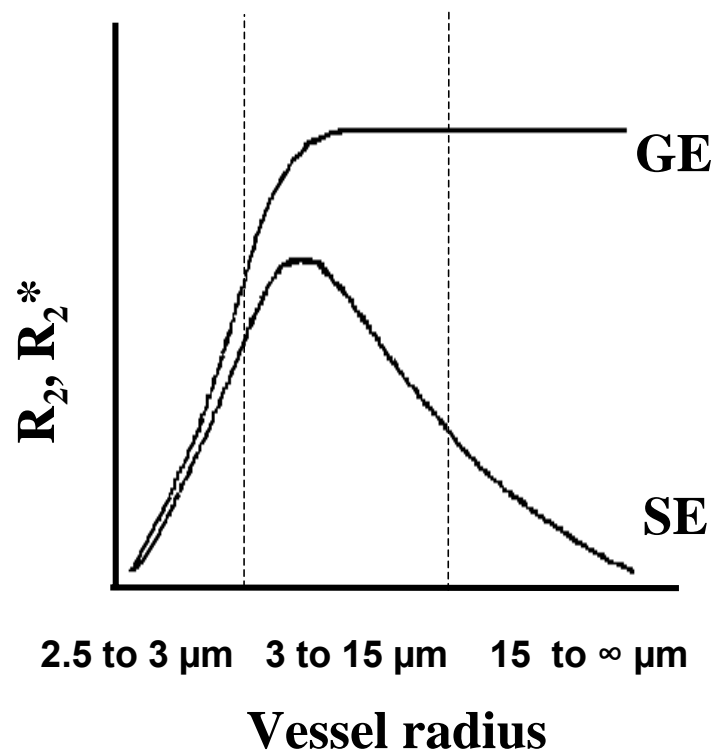
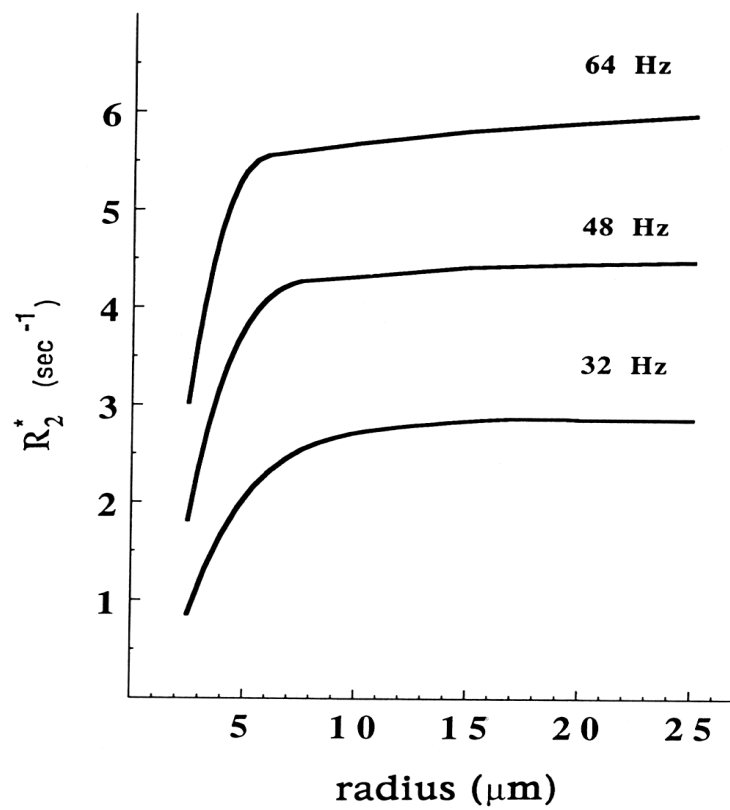
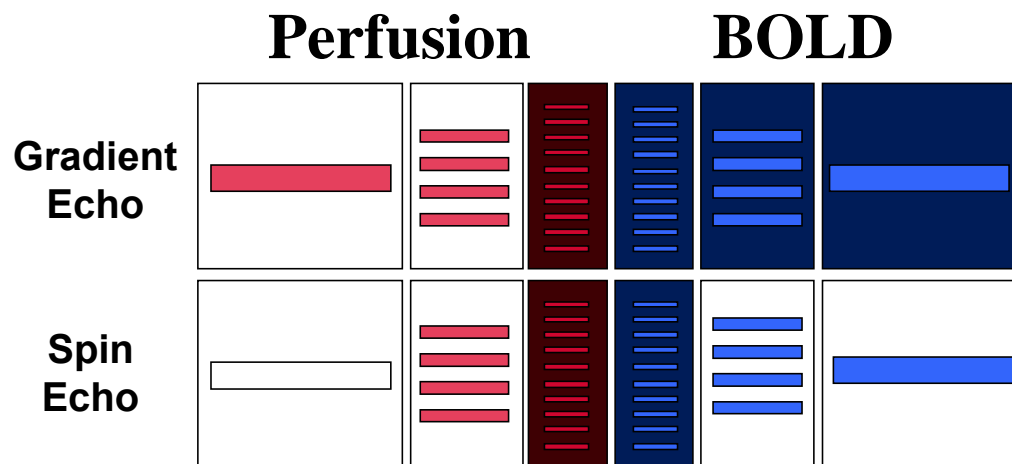


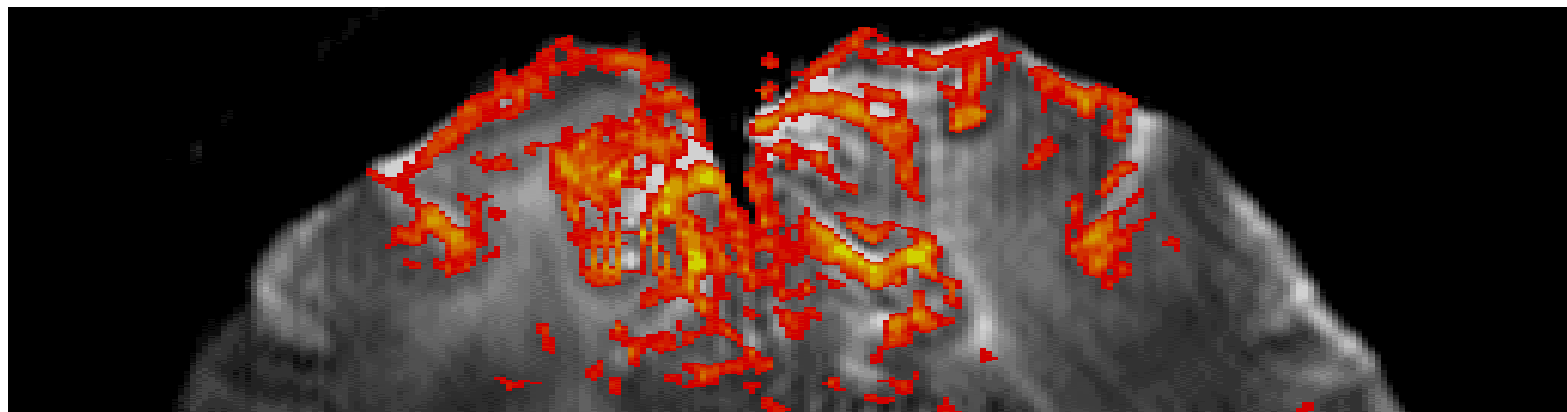
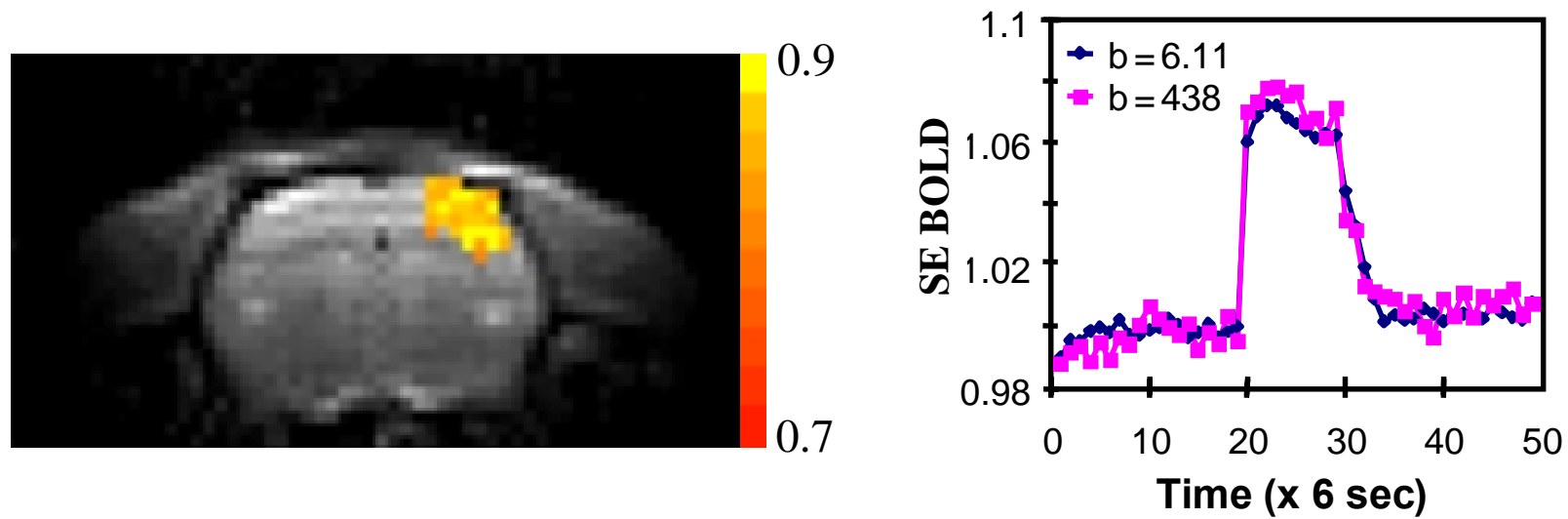
Fig. 9





Spatial
Heterogeneity





Relative Delay Time

